

Journal of Mechanics of Materials and Structures

**INVERSE PROBLEMS IN HETEROGENEOUS AND FRACTURED MEDIA
USING PERIDYNAMICS**

Daniel Z. Turner, Bart G. van Bloemen Waanders and Michael L. Parks

Volume 10, No. 5

December 2015



INVERSE PROBLEMS IN HETEROGENEOUS AND FRACTURED MEDIA USING PERIDYNAMICS

DANIEL Z. TURNER, BART G. VAN BLOEMEN WAANDERS AND MICHAEL L. PARKS

The following work presents an adjoint-based methodology for solving inverse problems in heterogeneous and fractured media using state-based peridynamics. We show that the inner product involving the peridynamic operators is self-adjoint. The proposed method is illustrated for several numerical examples with constant and spatially varying material parameters as well as in the context of fractures. We also present a framework for obtaining material parameters by integrating digital image correlation (DIC) with inverse analysis. This framework is demonstrated by evaluating the bulk and shear moduli for a sample of nuclear graphite using digital photographs taken during the experiment. The resulting measured values correspond well with other results reported in the literature. Lastly, we show that this framework can be used to determine the load state given observed measurements of a crack opening. This type of analysis has many applications in characterizing subsurface stress-state conditions given fracture patterns in cores of geologic material.

1. Introduction

Detecting fractures is important in many areas of engineering and geoscience. From material reliability to characterization of petroleum source rock, the goal is to predict the magnitude and orientation of fractures by calibrating the properties of numerical models so that eventually accurate predictions can be issued. Model calibration is a mathematical inversion process in which the differences between observations and numerical predictions are reconciled by perturbing model parameters such as boundary conditions, loadings, and material properties. Given a sufficient number of observations, accurate numerical models can be calculated, which in turn can then support the improvement of system design and operating conditions. In this paper, we are interested in solving inverse problems that determine loading conditions and material properties for fractured linear elasticity problems. Given calibrated numerical models, the design of engineering systems to ensure material reliability can be improved or more accurate flow patterns can increase the extraction of hydrocarbon in petroleum reservoirs. Various challenges arise in this type of an inversion problem, consisting of (1) achieving accurate and efficient modeling of fractures, (2) handling of large numbers of inversion parameters, (3) addressing sparsity of observations inherent in most large-scale inversion problems, (4) managing discontinuities from fractures, and (5) accounting for nonlinearities in the material inversion problem.

Our first challenge is to numerically model fractures accurately and efficiently in addition to being more conducive to the inverse setting. In particular, sensitivity objects will need to be extracted from the forward model to efficiently calculate the gradient as part of an optimization algorithm. Consequently, any approach must be able to generate derivatives with respect to the state variable (displacements in

Keywords: peridynamics, fractured media, inverse problems, digital image correlation.

the case of linear elasticity). To accommodate this prerequisite and model fractures, we leverage peridynamics, which has rapidly gained popularity as a nonlocal model for solid mechanics and naturally incorporates discontinuities (cracks). As opposed to partial derivative based models, integral equations are used instead, thereby avoiding differentiability requirements on the displacement field in the forward case. One of the goals of the paper is to demonstrate that this differentiability condition is not violated in the inverse setting. First introduced in 2000, peridynamics has been successfully applied in a number of areas [Silling 2000; Silling et al. 2007; Silling and Askari 2005; Silling and Lehoucq 2008]. The methodology has evolved from a bond- to a state-based approach to allow the modeling of more general linear elastic materials with Poisson's ratio other than $\frac{1}{4}$. Furthermore, this paper graduates peridynamics from a powerful forward modeling capability to, in some respects, an even more powerful inversion capability. Our inversion approach extends to other optimization formulations such as design and control problems.

The second and third challenges motivate the use of large-scale inversion techniques to solve a least square problem constrained by peridynamics. Also known as a constrained optimization problem or in the case of partial differential equation (PDE) based dynamics, PDE-constrained optimization [Akçelik et al. 2006], these techniques are designed to take advantage of embedded sensitivity calculations from the forward simulation to efficiently calculate the objective function gradient. For moderate numbers of inversion parameters, direct sensitivities can be used, but for large numbers of inversion variables, such as material properties, the size of which is equal to the number of degrees of freedom of the problem, an adjoint-based sensitivity calculation is required. In this paper, we explore the adjoint of peridynamics by leveraging nonlocal vector calculus (NLVC) [Du et al. 2013b] and demonstrate that the inner product of the forward operators with a vector is self-adjoint. Furthermore, we establish an inverse formulation based on the displacement of the material points without having to accommodate the so-called damage model that determines which broken bonds are part of a fracture. This addresses the fourth challenge, which identified a need to manage discontinuities from fractures.

The final challenge is addressed through the application of Newton-based optimization algorithms with line-search globalization and Tikhonov regularization to solve our target inverse problems. The constrained optimization problem is converted to an unconstrained formulation by forming a Lagrangian. Taking variations with respect to the state, Lagrange multipliers, and inversion parameters, the optimality conditions are derived. In the case of inverting for loading conditions, the optimality conditions are linear and therefore equal to the final Karush–Kuhn–Tucker (KKT) matrix. For material inversion, the optimality conditions are nonlinear and a linearization step via a Newton method is needed to arrive at the KKT system. In our numerical example, the observational data provides information at each computational node and therefore regularization does not dramatically improve the quality of the inversion. It should be noted that our solution techniques are applied to an unconstrained optimization problem by exercising a nonlinear elimination of the constraints. In subsequent sections of the paper, our derivation of the optimality conditions for a constrained optimization problem is primarily for presentational reasons; an alternative approach could be to differentiate the unconstrained objective function and apply the chain rule. With additional algebraic manipulations, the adjoint equation could be derived [van Bloemen Waanders et al. 2005].

The observational data in our numerical examples comes from digital image correlation (DIC), which is a noncontact, full-field displacement measurement technique. DIC uses digital images of the experimental sample to determine deformations [Sutton et al. 2009; Chu et al. 1985; Pan et al. 2009; Hild

and Roux 2006]. The process works by correlating subsets of pixels from an image of the undeformed experimental sample to a subset of an image of the deformed sample. This technique provides a much richer set of displacement data than would otherwise be possible using mechanical gauges. We use DIC to provide the observations of the material behavior, which are subsequently used in the objective function of the optimization. Using optimization, we determine the material parameter values that lead to the best fit between the simulated displacement field and the displacement field obtained.

The backdrop of this work is in the field of materials characterization, and we build upon a number of previous works. Of particular interest are those that investigate heterogeneous or structurally damaged media. Hild and Roux [2006] review various methods for material property identification using several different flavors of DIC. Grédiac [2004] evaluates the efficacy of DIC-based methods for composite materials. An anisotropic damage law is calibrated using DIC by Périé et al. [2009], who show that the proposed method obtains close correlation even under significant noise.

It will be important to distinguish the emphasis of this work on materials characterization for fractured media rather than determining fracture parameters using inversion. Asmaro [2013] uses a similar integration of DIC and inversion to obtain fracture parameters for concrete materials. Her inversion process is based on a finite element model that uses hinge elements. Many of the difficulties encountered in this approach are circumvented in this work through the use of peridynamics, which more naturally incorporates cracks.

This work makes the following contributions:

- Solutions of the inverse problem are presented for state-based peridynamics using an adjoint-based method.
- Inversions demonstrate the state of material loading given fracture parameters such as crack aperture.
- A novel framework is presented for determining material parameters by integrating DIC with peridynamics inverse analysis.
- The applicability of this framework is shown for heterogeneous materials where the material parameters vary throughout the problem domain.

In the sections that follow, we briefly summarize state-based peridynamics, define the constrained optimization problem and optimality conditions that represent the peridynamics inverse problem, and verify the proposed methodology for a material inversion and a loading inversion in the context of a fractured medium. We demonstrate the framework for incorporating digital image correlation by analyzing a compact tension specimen of nuclear graphite.

2. State-based peridynamics

Peridynamics was introduced as a framework to address the shortcomings of PDE-based approaches in which material discontinuities are not conveniently handled. The integral representation of the force calculation between material points avoids the problem of differentiating through a discontinuity. Although recent extensions to finite element methods have been introduced to address these issues, it is not clear if these methods can address the inverse problem and achieve either differentiability or computational efficiency for the inverse problem. In the next two sections, we outline the basic peridynamics formulation and map this approach to the inverse setting.

The peridynamic state-based balance of linear momentum is written as

$$\rho \ddot{\mathbf{u}} = \int_{\mathcal{H}_x} \{ \underline{\mathbf{T}}[\mathbf{x}]\langle \mathbf{x}' - \mathbf{x} \rangle - \underline{\mathbf{T}}[\mathbf{x}']\langle \mathbf{x} - \mathbf{x}' \rangle \} dV_{x'} + \mathbf{b}(\mathbf{x}), \quad (1)$$

where $\underline{\mathbf{T}}$ is the force state and $\mathbf{b}(\mathbf{x})$ is a volumetric force. Here we use the underline notation to denote a state, which can be conceptualized as a scalar, vector, or tensor quantity of interest that involves a convolution with values of this field in the neighborhood of the material point in question. One can think of a state as being a quantity that derives its value from a sum of contributions over the region surrounding point \mathbf{x} . Within a spherical neighborhood, \mathcal{H}_x , of a material point at \mathbf{x} , the force interactions between \mathbf{x} and all other material points inside the neighborhood are nonzero. We use the state-based formulation for peridynamics to avoid the well-known restrictions on the material parameters that result from the bond-based formulation. The convention $\langle \mathbf{x}' - \mathbf{x} \rangle$ denotes a bond between points \mathbf{x} and \mathbf{x}' . The original scalar length of a bond is denoted, \underline{x} . The current length of a bond is denoted, \underline{y} , and is a function of the displacement field, $\mathbf{u}(\mathbf{x})$. Without loss of generality, we ignore the inertial term and focus our attention on quasistatic analysis as this will clarify the presentation. Neglecting the inertial term has no impact on the development of the inversion process and can easily be reintroduced to obtain transient quantities. The quasistatic governing equations can be written in terms of the linear peridynamic operator, $\mathcal{L}\mathbf{u}$

$$\mathcal{L}\mathbf{u}(\mathbf{x}) + \mathbf{b}(\mathbf{x}) = 0 \quad \text{in } \Omega \subset \mathbb{R}^d \quad (2)$$

where

$$\mathcal{L}\mathbf{u}(\mathbf{x}) := \int_{\mathcal{H}_x} \{ \underline{\mathbf{T}}[\mathbf{x}]\langle \mathbf{x}' - \mathbf{x} \rangle - \underline{\mathbf{T}}[\mathbf{x}']\langle \mathbf{x} - \mathbf{x}' \rangle \} dV_{x'}, \quad (3)$$

d is the spatial dimension and Ω is the domain. Readers unfamiliar with the notation of state-based peridynamics should consult [Silling et al. 2007] in which the state-based formulation is presented. In general, a peridynamic state produces a quantity from a summation of values over a material point's family. In the case of the force state, the resulting vector is the force density at a point given the interactions with all the bonds in the family. For an ordinary material, the force between material points acts along a unit vector between the two points in the deformed configuration (as shown at the top of Figure 1) such that the force state can be expressed as

$$\underline{\mathbf{T}} = \underline{t} \underline{\mathbf{M}}, \quad (4)$$

where $\underline{\mathbf{M}}$ is the unit vector pointing from $\mathbf{x} + \mathbf{u}(\mathbf{x})$ to $\mathbf{x}' + \mathbf{u}(\mathbf{x}')$ and \underline{t} is the scalar force state.

For a linear, elastic material (parametrized by k and μ), in plane-strain, the constitutive relationship between the scalar force state and the deformation is

$$\underline{t} = \tilde{k} \left(\frac{2\theta}{m} \underline{x} \right) + \tilde{\alpha} \left(\underline{y} - \underline{x} \left(1 + \frac{\theta}{2} \right) \right), \quad (5)$$

where m is the weighted size

$$m = \int_{\mathcal{H}_x} \underline{x}^2 dV_{x'}, \quad (6)$$

θ is the dilatation

$$\theta = \frac{2}{m} \int_{\mathcal{H}_x} (\underline{y} - \underline{x}) \underline{x} dV_{x'}, \quad (7)$$

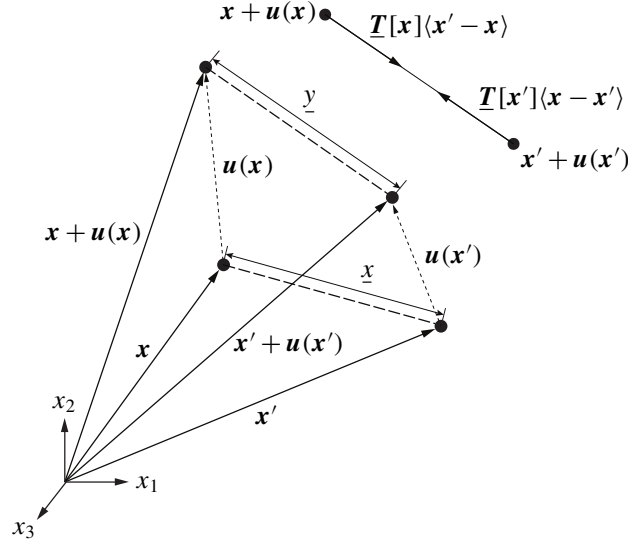


Figure 1. Geometry of deformation for peridynamics. This figure shows a bond between two material points as it evolves from the reference to the deformed configuration. The nodes in the figure above represent the cell centroids in the discretization of peridynamics. The cells surrounding each node are not drawn in this figure. The force-state interaction of these two material points is shown in the top of the figure which illustrates that the resulting forces align with the bond between the material points. Here we are using an ordinary material formulation in which the force between material points is always directed along the bond between them.

and the coefficients are $\tilde{k} = (k + \mu/9)$ and $\tilde{\alpha} = 8\mu/m$. (Here we are using the two-dimensional formulation proposed in [Le et al. 2014]. Extending this formulation to three dimensions is trivial.)

In the discrete setting, using single point quadrature, (1) becomes¹

$$c(\mathbf{u}, k, \mu) \equiv \sum_{i=1}^{N_x} \{ \underline{\mathbf{T}}[\mathbf{x}]\langle \mathbf{x}'_i - \mathbf{x} \rangle - \underline{\mathbf{T}}[\mathbf{x}'_i]\langle \mathbf{x} - \mathbf{x}'_i \rangle \} V_{x_i} + \mathbf{b}(\mathbf{x}) = 0 \tag{8}$$

for all points in the domain, where N_x is the number of discrete neighbors of \mathbf{x} in \mathcal{H}_x and V_{x_i} is the cell area of neighbor i . The structure of (8) is important from the perspective that it preserves symmetry of the resulting tangent matrix. This ensures that the discrete operator, \mathbf{J}_u (to be defined below) has the following property, $\mathbf{J}_u = \mathbf{J}_u^T$, even if the material parameters vary throughout the domain, for example $k(\mathbf{x}) \neq k(\mathbf{x}')$. Also note that the quantities θ and \underline{y} are dependent on the peridynamic displacement field, \mathbf{u} .

¹Note that in the formulation above we have used a constant, unit, influence function ($\underline{w} = 1$), which we have omitted for brevity.

The weighted size and dilatation are computed in the discrete setting as

$$m = \sum_{i=1}^N \underline{x}^2 V_{x'_i}, \quad (9)$$

$$\theta = \frac{2}{m} \sum_{i=1}^N (\underline{y} - \underline{x}) \underline{x} V_{x'_i}. \quad (10)$$

3. Peridynamics inverse problem

In this section, our optimization problem is formulated, the optimality conditions are derived, and we prove that the inner product involving the forward operators is self-adjoint. This realization has obvious benefits to implementing the inverse process.

3.1. Inverse problem. The inverse problem can be stated as the following nonlinear, constrained, least squares optimization problem:

$$\min_{\mathbf{u}, k, \mu} g(\mathbf{u}, k, \mu) \quad \text{subject to} \quad \begin{cases} \mathbf{c}(\mathbf{u}, k, \mu) = \mathbf{0} & \text{in } \Omega, \\ \mathbf{u} = \mathbf{u}_0 & \text{in } \Omega^u, \\ \mathbf{b} = \mathbf{q} & \text{in } \Omega^q \end{cases} \quad (11)$$

where $\mathbf{c}(\mathbf{u}, k, \mu)$ is the constraint equation given by (8). Ω^u and Ω^q are the volume constraint regions for displacement and loading, respectively. Note that as opposed to traditional boundary value problems in which the boundary conditions are prescribed over a surface, in peridynamics, the boundary conditions are prescribed over a volume. Typically, to represent a displacement boundary condition, rather than apply a prescribed displacement on the surface nodes, ghost cells are added to the domain at the boundary, for which the displacement is given. For loading boundary conditions, the prescribed load is distributed among a collection of cells interior to the domain. The above problem is nonlinear due to the constraint equation's dependence on the decision variables.² We employ a least squares misfit of the computed displacements with a set of observed displacements, \mathbf{u}^* , at N_{obs} observation points, as our objective function, $g(\mathbf{u}, k, \mu)$, with Tikhonov regularization [Tikhonov and Arsenin 1977]:

$$g(\mathbf{u}, k, \mu) = \frac{1}{2} \sum_{j=1}^{N_{\text{obs}}} \int_{\Omega} ((u_x - u_x^*)^2 + (u_y - u_y^*)^2) \delta(\mathbf{x} - \mathbf{x}_j) d\Omega + \frac{\psi_k}{2} \int_{\Omega} k^2 d\Omega + \frac{\psi_{\mu}}{2} \int_{\Omega} \mu^2 d\Omega. \quad (12)$$

In the objective function above, Ω represents the problem domain, ψ_k and ψ_{μ} are the regularization parameters and δ is the Dirac delta. We wish to invert the system of state-based peridynamics equations above for the material parameters k and μ , which represent our *decision* variables. The parameters ψ_{μ} and ψ_k represent tunable parameters that drive the optimization process to a unique solution. The third and fourth terms in the functional provide that for large values of ψ_{μ} and ψ_k the functional is quadratic in nature.

²Formally speaking, since we solve the above system in a staggered fashion, it would be more appropriate to denote the minimization problem as $\text{ming}(\mathbf{u}(k, \mu))$ where \mathbf{u} satisfies $\mathbf{c}(\mathbf{u}(k, \mu)) = 0$.

3.2. Optimality conditions. Introducing the Lagrange multiplier field, $\lambda(\mathbf{x})$ (the adjoint variable) the following Lagrangian functional can be constructed using the inner product

$$L(\mathbf{u}, \lambda, \mathbf{d}) := g(\mathbf{u}, \mathbf{d}) + \int_{\Omega} \mathbf{c} \cdot \lambda - \mathbf{d} \cdot \lambda \, dx, \tag{13}$$

where \mathbf{d} represents the decision variables that include k and μ . Linearizing the peridynamic operator and taking variations of $L(\mathbf{u}, \lambda, \mathbf{d})$ with respect to \mathbf{u} , \mathbf{d} and λ produces optimality conditions given below. It can be shown that taking the variation with respect to \mathbf{u} leads to $\mathcal{L}^* = \mathbf{J}_u = \partial \mathbf{c} / \partial \mathbf{u}$, i.e. that the peridynamic operator is self-adjoint, the proof of which is demonstrated in the following section.

The optimality conditions for (11) are as follows:

$$\mathbf{c} = \mathbf{0} \quad \text{in } \Omega \quad (\text{state}), \tag{14}$$

$$\mathbf{J}_u^T \lambda + \mathbf{g}_u = \mathbf{0} \quad \text{in } \Omega \quad (\text{adjoint}), \tag{15}$$

$$\mathbf{J}_d^T \lambda + \mathbf{g}_d = \mathbf{0} \quad \text{in } \Omega \quad (\text{decision}). \tag{16}$$

In the discrete context, $\mathbf{u} \in \mathbb{R}^M$ is the state variable vector, $\lambda \in \mathbb{R}^M$ is the adjoint variable vector, and $\mathbf{d} \in \mathbb{R}^P$ is the decision variable vector. For the numerical examples that follow, the decision vector is assembled as a single column vector

$$\mathbf{d} = \begin{bmatrix} k_1 \\ \vdots \\ k_{P/2} \\ \mu_1 \\ \vdots \\ \mu_{P/2} \end{bmatrix}. \tag{17}$$

The other terms in the optimality conditions include: $\mathbf{J}_u = \partial \mathbf{c} / \partial \mathbf{u} \in \mathbb{R}^{M \times M}$ which is a matrix that represents the variation of the constraint with respect to the state variables; $\mathbf{J}_d = \partial \mathbf{c} / \partial \mathbf{d} \in \mathbb{R}^{M \times P}$, a matrix that represents the variation of the constraint with respect to the decision variables; $\mathbf{g}_u = \partial g / \partial \mathbf{u} \in \mathbb{R}^M$, and $\mathbf{g}_d = \partial g / \partial \mathbf{d} \in \mathbb{R}^P$, that represent the sensitivity of the objective function to the state and decision variables, respectively.

In addition to the optimization problem being nonlinear, the state equation is also nonlinear due to the dependence of the displacement at \mathbf{x} on the displacement at \mathbf{x}' (hence the nonlocal nature of peridynamics). To treat this complexity, in the calculation of \mathbf{J}_u , we first linearize the state equation and compute \mathbf{J}_u using central finite differencing. The above optimization problem can be solved using a variety of methods. For the numerical examples that follow, a reflective trust-region algorithm was used with a conjugate gradient solver. For any given method, the gradient of the objective function with respect to the decision variables, $\nabla_d(g) = dg/d\mathbf{d}$, must be computed. To compute $\nabla_d(g)$, the following algorithm was used. First, the adjoint equation is solved for λ , as

$$\lambda = -\mathbf{J}_u^{-T} \mathbf{g}_u. \tag{18}$$

Once the adjoint variables are determined, the gradient of the objective function can be computed as

$$\nabla_d(g) = -\mathbf{g}_d - \mathbf{J}_d^T \boldsymbol{\lambda}. \quad (19)$$

3.3. Self-adjointness of the peridynamic operator. The self-adjointness of \mathcal{L} is not immediately obvious given the state-based representation of peridynamics. The state-based formulation involves a multilayered convolution, the first is used to obtain the dilatation which is then convolved for the force state. To prove this property we turn to NLVC [Du et al. 2013a; Gunzburger and Lehoucq 2010; Du et al. 2013b; Alali et al. 2014] in an effort to analyze the peridynamic operator in a more straightforward manner. The self-adjointness of peridynamics on bounded domains has also been studied in [Mengesha and Du 2014; 2015]. NLVC is a recently introduced formalism with appropriate nonlocal corollaries to all of the components of local balance laws. In addition, NLVC can be used to cast nonlocal theories (like peridynamics) in a more abstract and general mathematical setting which is more amenable to analysis. Following the presentation in [Alali et al. 2014], the peridynamics operator, \mathcal{L} from (2) can be written as

$$\mathcal{L}\mathbf{u} = -\mathcal{G}(c_1 \mathcal{G}^* \mathbf{u}) - \mathcal{G}(c_2 \overline{\mathcal{G}^*} \mathbf{u}), \quad (20)$$

where \mathcal{G} , \mathcal{G}^* and $\overline{\mathcal{G}^*}$ are defined as the nonlocal gradient operator, the adjoint of the nonlocal gradient operator and the average of the adjoint, respectively. For a scalar function $\xi(\mathbf{x}, \mathbf{y})$ these are given as

$$(\mathcal{G}\xi)(\mathbf{x}) = \int_{\mathbb{R}^d} (\xi(\mathbf{y}, \mathbf{x}) + \xi(\mathbf{x}, \mathbf{y})) \boldsymbol{\alpha}(\mathbf{x}, \mathbf{y}) d\mathbf{y}, \quad (21)$$

$$(\mathcal{G}^* \mathbf{u}) = -(\mathbf{u}(\mathbf{y}) - \mathbf{u}(\mathbf{x})) \cdot \boldsymbol{\alpha}(\mathbf{x}, \mathbf{y}), \quad (22)$$

$$(\overline{\mathcal{G}^*} \mathbf{u})(\mathbf{x}) = - \int_{\mathbb{R}^d} (\mathbf{u}(\mathbf{y}) - \mathbf{u}(\mathbf{x})) \cdot \boldsymbol{\alpha}(\mathbf{x}, \mathbf{y}) d\mathbf{y}, \quad (23)$$

where $\boldsymbol{\alpha}(\mathbf{x}, \mathbf{y})$ is an appropriate antisymmetric vector-valued kernel ($\boldsymbol{\alpha}(\mathbf{x}, \mathbf{y}) = -\boldsymbol{\alpha}(\mathbf{y}, \mathbf{x})$). We have cast the peridynamic equations in the NLVC setting to derive the adjoint of \mathcal{L} , denoted as \mathcal{L}^* . Given the function spaces and duality pairings defined in [Alali et al. 2014], the adjoint of the peridynamic operator is defined such that it satisfies

$$\langle \mathbf{v}, \mathcal{L}\mathbf{u} \rangle = \langle \mathbf{u}, \mathcal{L}^* \mathbf{v} \rangle, \quad (24)$$

where $\langle \cdot, \cdot \rangle$ is the vector inner product, given by $\langle \mathbf{a}(\mathbf{x}), \mathbf{b}(\mathbf{x}) \rangle = \int_{\mathbb{R}^d} \mathbf{a}(\mathbf{x}) \cdot \mathbf{b}(\mathbf{x}) d\mathbf{x}$. Expanding the terms of (20), gives

$$\mathcal{G}(c_1 \mathcal{G}^* \mathbf{u}) = - \int_{\mathbb{R}^d} [c_1(\mathbf{y})(\mathbf{u}(\mathbf{x}) - \mathbf{u}(\mathbf{y})) \cdot \boldsymbol{\alpha}(\mathbf{y}, \mathbf{x}) + c_1(\mathbf{x})(\mathbf{u}(\mathbf{y}) - \mathbf{u}(\mathbf{x})) \cdot \boldsymbol{\alpha}(\mathbf{x}, \mathbf{y})] \boldsymbol{\alpha}(\mathbf{x}, \mathbf{y}) d\mathbf{y},$$

$$\mathcal{G}(c_2 \overline{\mathcal{G}^*} \mathbf{u}) = - \int_{\mathbb{R}^d} \left[c_2(\mathbf{y}) \int_{\mathbb{R}^d} (\mathbf{u}(\mathbf{z}) - \mathbf{u}(\mathbf{y})) \cdot \boldsymbol{\alpha}(\mathbf{y}, \mathbf{z}) d\mathbf{z} + c_2(\mathbf{x}) \int_{\mathbb{R}^d} (\mathbf{u}(\mathbf{z}) - \mathbf{u}(\mathbf{x})) \cdot \boldsymbol{\alpha}(\mathbf{x}, \mathbf{z}) d\mathbf{z} \right] \boldsymbol{\alpha}(\mathbf{x}, \mathbf{y}) d\mathbf{y}.$$

The inner product of $\mathcal{L}\mathbf{u}$ and \mathbf{v} is then

$$\begin{aligned} \langle \mathbf{v}, \mathcal{L}\mathbf{u} \rangle &= \int_{\mathbb{R}^d} \int_{\mathbb{R}^d} [c_1(\mathbf{y})(\mathbf{u}(\mathbf{x}) - \mathbf{u}(\mathbf{y})) \cdot \boldsymbol{\alpha}(\mathbf{y}, \mathbf{x}) + c_1(\mathbf{x})(\mathbf{u}(\mathbf{y}) - \mathbf{u}(\mathbf{x})) \cdot \boldsymbol{\alpha}(\mathbf{x}, \mathbf{y})] \boldsymbol{\alpha}(\mathbf{x}, \mathbf{y}) \cdot \mathbf{v}(\mathbf{x}) d\mathbf{x} d\mathbf{y} \\ &+ \int_{\mathbb{R}^d} \int_{\mathbb{R}^d} \left[c_2(\mathbf{y}) \int_{\mathbb{R}^d} (\mathbf{u}(\mathbf{z}) - \mathbf{u}(\mathbf{y})) \cdot \boldsymbol{\alpha}(\mathbf{y}, \mathbf{z}) d\mathbf{z} + c_2(\mathbf{x}) \int_{\mathbb{R}^d} (\mathbf{u}(\mathbf{z}) - \mathbf{u}(\mathbf{x})) \cdot \boldsymbol{\alpha}(\mathbf{x}, \mathbf{z}) d\mathbf{z} \right] \boldsymbol{\alpha}(\mathbf{x}, \mathbf{y}) \cdot \mathbf{v}(\mathbf{x}) d\mathbf{x} d\mathbf{y}. \end{aligned}$$

Expanding all terms in the inner product gives

$$\begin{aligned}
 \langle \mathbf{v}, \mathcal{L}\mathbf{u} \rangle &= \int_{\mathbb{R}^d} \int_{\mathbb{R}^d} c_1(\mathbf{y})(\mathbf{u}(\mathbf{x}) \cdot \boldsymbol{\alpha}(\mathbf{y}, \mathbf{x}))(\boldsymbol{\alpha}(\mathbf{x}, \mathbf{y}) \cdot \mathbf{v}(\mathbf{x})) \, d\mathbf{x} \, d\mathbf{y} \\
 &\quad - \int_{\mathbb{R}^d} \int_{\mathbb{R}^d} c_1(\mathbf{y})(\mathbf{u}(\mathbf{y}) \cdot \boldsymbol{\alpha}(\mathbf{y}, \mathbf{x}))(\boldsymbol{\alpha}(\mathbf{x}, \mathbf{y}) \cdot \mathbf{v}(\mathbf{x})) \, d\mathbf{x} \, d\mathbf{y} \\
 &\quad + \int_{\mathbb{R}^d} \int_{\mathbb{R}^d} c_1(\mathbf{x})(\mathbf{u}(\mathbf{y}) \cdot \boldsymbol{\alpha}(\mathbf{x}, \mathbf{y}))(\boldsymbol{\alpha}(\mathbf{x}, \mathbf{y}) \cdot \mathbf{v}(\mathbf{x})) \, d\mathbf{x} \, d\mathbf{y} \\
 &\quad - \int_{\mathbb{R}^d} \int_{\mathbb{R}^d} c_1(\mathbf{x})(\mathbf{u}(\mathbf{x}) \cdot \boldsymbol{\alpha}(\mathbf{x}, \mathbf{y}))(\boldsymbol{\alpha}(\mathbf{x}, \mathbf{y}) \cdot \mathbf{v}(\mathbf{x})) \, d\mathbf{x} \, d\mathbf{y} \\
 &\quad + \int_{\mathbb{R}^d} \int_{\mathbb{R}^d} c_2(\mathbf{y}) \int_{\mathbb{R}^d} (\mathbf{u}(\mathbf{z}) \cdot \boldsymbol{\alpha}(\mathbf{y}, \mathbf{z})) \, d\mathbf{z} (\boldsymbol{\alpha}(\mathbf{x}, \mathbf{y}) \cdot \mathbf{v}(\mathbf{x})) \, d\mathbf{x} \, d\mathbf{y} \\
 &\quad - \int_{\mathbb{R}^d} \int_{\mathbb{R}^d} c_2(\mathbf{y}) \int_{\mathbb{R}^d} (\mathbf{u}(\mathbf{y}) \cdot \boldsymbol{\alpha}(\mathbf{y}, \mathbf{z})) \, d\mathbf{z} (\boldsymbol{\alpha}(\mathbf{x}, \mathbf{y}) \cdot \mathbf{v}(\mathbf{x})) \, d\mathbf{x} \, d\mathbf{y} \\
 &\quad + \int_{\mathbb{R}^d} \int_{\mathbb{R}^d} c_2(\mathbf{x}) \int_{\mathbb{R}^d} (\mathbf{u}(\mathbf{z}) \cdot \boldsymbol{\alpha}(\mathbf{x}, \mathbf{z})) \, d\mathbf{z} (\boldsymbol{\alpha}(\mathbf{x}, \mathbf{y}) \cdot \mathbf{v}(\mathbf{x})) \, d\mathbf{x} \, d\mathbf{y} \\
 &\quad - \int_{\mathbb{R}^d} \int_{\mathbb{R}^d} c_2(\mathbf{x}) \int_{\mathbb{R}^d} (\mathbf{u}(\mathbf{x}) \cdot \boldsymbol{\alpha}(\mathbf{x}, \mathbf{z})) \, d\mathbf{z} (\boldsymbol{\alpha}(\mathbf{x}, \mathbf{y}) \cdot \mathbf{v}(\mathbf{x})) \, d\mathbf{x} \, d\mathbf{y}.
 \end{aligned}$$

Using the antisymmetry of $\boldsymbol{\alpha}(\mathbf{x}, \mathbf{y})$ and a change of variable from $\mathbf{x} \rightarrow \mathbf{y}$ in some of the terms above leads to

$$\begin{aligned}
 \langle \mathbf{v}, \mathcal{L}\mathbf{u} \rangle &= \int_{\mathbb{R}^d} \int_{\mathbb{R}^d} c_1(\mathbf{y})(\mathbf{u}(\mathbf{x}) \cdot \boldsymbol{\alpha}(\mathbf{y}, \mathbf{x}))(\boldsymbol{\alpha}(\mathbf{x}, \mathbf{y}) \cdot \mathbf{v}(\mathbf{x})) \, d\mathbf{x} \, d\mathbf{y} \\
 &\quad \times \int_{\mathbb{R}^d} \int_{\mathbb{R}^d} c_1(\mathbf{x})(\mathbf{u}(\mathbf{x}) \cdot \boldsymbol{\alpha}(\mathbf{x}, \mathbf{y}))(\boldsymbol{\alpha}(\mathbf{x}, \mathbf{y}) \cdot \mathbf{v}(\mathbf{y})) \, d\mathbf{x} \, d\mathbf{y} \\
 &\quad - \int_{\mathbb{R}^d} \int_{\mathbb{R}^d} c_1(\mathbf{y})(\mathbf{u}(\mathbf{x}) \cdot \boldsymbol{\alpha}(\mathbf{x}, \mathbf{y}))(\boldsymbol{\alpha}(\mathbf{y}, \mathbf{x}) \cdot \mathbf{v}(\mathbf{y})) \, d\mathbf{x} \, d\mathbf{y} \\
 &\quad - \int_{\mathbb{R}^d} \int_{\mathbb{R}^d} c_1(\mathbf{x})(\mathbf{u}(\mathbf{x}) \cdot \boldsymbol{\alpha}(\mathbf{x}, \mathbf{y}))(\boldsymbol{\alpha}(\mathbf{x}, \mathbf{y}) \cdot \mathbf{v}(\mathbf{x})) \, d\mathbf{x} \, d\mathbf{y} \\
 &\quad + \int_{\mathbb{R}^d} \int_{\mathbb{R}^d} \int_{\mathbb{R}^d} c_2(\mathbf{y})(\mathbf{u}(\mathbf{x}) \cdot \boldsymbol{\alpha}(\mathbf{x}, \mathbf{y}))(\boldsymbol{\alpha}(\mathbf{y}, \mathbf{z}) \cdot \mathbf{v}(\mathbf{z})) \, d\mathbf{z} \, d\mathbf{x} \, d\mathbf{y} \\
 &\quad - \int_{\mathbb{R}^d} \int_{\mathbb{R}^d} \int_{\mathbb{R}^d} c_2(\mathbf{y})(\mathbf{u}(\mathbf{x}) \cdot \boldsymbol{\alpha}(\mathbf{x}, \mathbf{y}))(\boldsymbol{\alpha}(\mathbf{y}, \mathbf{z}) \cdot \mathbf{v}(\mathbf{y})) \, d\mathbf{z} \, d\mathbf{x} \, d\mathbf{y} \\
 &\quad + \int_{\mathbb{R}^d} \int_{\mathbb{R}^d} \int_{\mathbb{R}^d} c_2(\mathbf{x})(\mathbf{u}(\mathbf{x}) \cdot \boldsymbol{\alpha}(\mathbf{x}, \mathbf{y}))(\boldsymbol{\alpha}(\mathbf{x}, \mathbf{z}) \cdot \mathbf{v}(\mathbf{z})) \, d\mathbf{z} \, d\mathbf{x} \, d\mathbf{y} \\
 &\quad - \int_{\mathbb{R}^d} \int_{\mathbb{R}^d} \int_{\mathbb{R}^d} c_2(\mathbf{x})(\mathbf{u}(\mathbf{x}) \cdot \boldsymbol{\alpha}(\mathbf{x}, \mathbf{y}))(\boldsymbol{\alpha}(\mathbf{x}, \mathbf{z}) \cdot \mathbf{v}(\mathbf{x})) \, d\mathbf{z} \, d\mathbf{x} \, d\mathbf{y} \\
 &= \langle \mathbf{u}, \mathcal{L}^*\mathbf{v} \rangle.
 \end{aligned}$$

Here we have shown that the peridynamic operator is self-adjoint, i.e.,

$$\mathcal{L}^* = \mathcal{L}^T = \mathcal{L}. \tag{25}$$

Parameter	Exact	Computed	Error (%)
k	666.67	666.67	0.0000644
μ	400.0	399.9984	0.000395

Table 1. Results for the constant material parameter verification problem.

4. Numerical examples

We present here three illustrative examples that demonstrate the effectiveness of the proposed method. The first problem is a verification problem in which the parameters k and μ are determined as constants for the entire domain (nonspatially varying) and compared with the exact result. In the second problem we invert for a spatially varying, heterogeneous material parameter $\mu(x)$ and compare the result with the exact solution. In the last problem, digital image correlation is used to experimentally determine k and μ for a sample of nuclear graphite in a compact tension test.

4.1. Verification for constant material parameters. Consider a 2D, square domain $\Omega \in \mathbb{R}^{L \times L}$, where $L = 1000$, subjected to zero displacement along the bottom edge ($y = 0$) and an applied force in the x and y directions, $F_x = 1000.0$ and $F_y = 1000.0$, respectively, along the top edge as shown in Figure 2.³ For this problem, the observed displacement field, \mathbf{u}^* , was manufactured by solving the forward problem with $k = 666.67$ and $\mu = 400.0$. Both material parameters were held constant over the domain (i.e. $P = 2$). The goal of this inverse problem is to solve for the constants k and μ , given the loading and least squares misfit of the computed displacement field, \mathbf{u} , to the observed displacement field, \mathbf{u}^* , using the objective function defined by (12). For this problem no regularization was used ($\psi_k = 0$ and $\psi_\mu = 0$).

The domain was discretized into cells of size $h \times h$, where $h = 100.0$.⁴ The initial guess for k and μ were seeded with values of 100.0 and 100.0, respectively. Table 1 shows the results for this example. The results suggest that constant parameters can be inverted for with great accuracy using the methodology above. The convergence of the objective function is plotted in Figure 3.

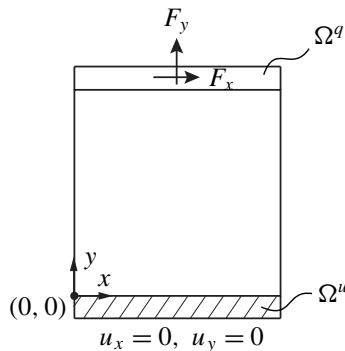


Figure 2. Domain and boundary conditions for academic verification problems.

³The force is applied by distributing the magnitude of the force over the cells along the top edge of the domain and adding the value to the momentum balance residual (8) for each point. As the horizon increases, the force is distributed over a layer of points near the boundary of thickness, δ .

⁴Along the boundary, the centroid of the cell was placed on the edge of the domain such that $h = 10.0$ results in 11 cells in x and y , or 121 cells total.

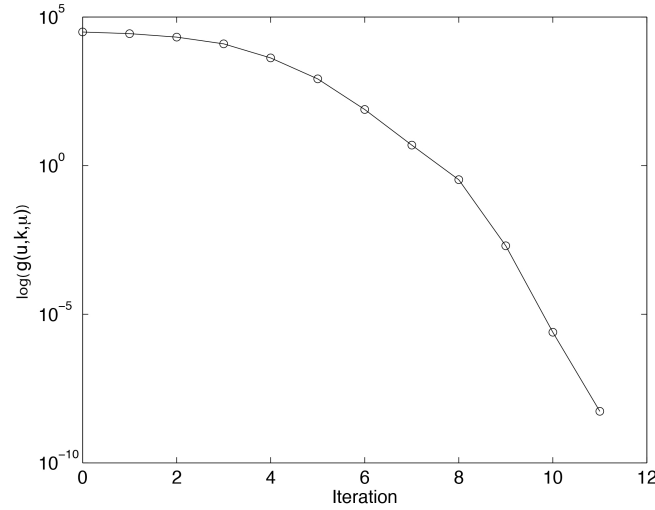


Figure 3. Convergence of the objective function per iteration for the constant material parameters problem. The y-axis is $\log(g(u, k, \mu))$.

4.2. Inversion for heterogeneous material properties. In this example we invert for $\mu(\mathbf{x})$, a spatially varying material parameter, using the same domain and boundary conditions shown in Figure 2. The value of μ is determined for every cell in the domain (i.e. $P = 121$). Observed values of displacement were populated using the following material parameters, which represent the exact solution.

$$k(\mathbf{x}) = -\gamma_k r k_0 + k_0, \tag{26}$$

$$\mu(\mathbf{x}) = \gamma_\mu r \mu_0 + \mu_0 \tag{27}$$

where $r = \|\mathbf{x}\|$, $\gamma_k = 0.00025$, $\gamma_\mu = 0.0002$, $k_0 = 666.67$ and $\mu_0 = 400.0$. The initial guess for \mathbf{d} was seeded with a constant $\mu = \mu_0$ throughout the domain. Note that we only solve for $\mu(\mathbf{x})$ and not $k(\mathbf{x})$.

A comparison between the computed result and the exact solution is shown in Figure 4. The maximum error in the computed solution is 1.2%. These results suggest that the method above is effective for constant material parameters as well as spatially varying fields. A plot of the convergence of the objective function for each iteration is shown in Figure 5.

4.3. Inversion for material parameters using digital image correlation data. The last example illustrates the proposed method’s usefulness in determining material parameters by inversion using experimental data generated with digital image correlation. For this example, the parameters k and μ are determined for a sample of (nonirradiated) nuclear graphite loaded in a compact tension test. The boundary conditions for the problem are established by using the digital image correlation displacements as a prescribed displacement over a thin layer of cells that circumscribe the area of interest. To simplify the analysis, the parameters are evaluated for a load state early in the loading cycle before nonlinear behavior is present. A picture of the experimental setup is shown in Figure 6. The setup involves a single axis

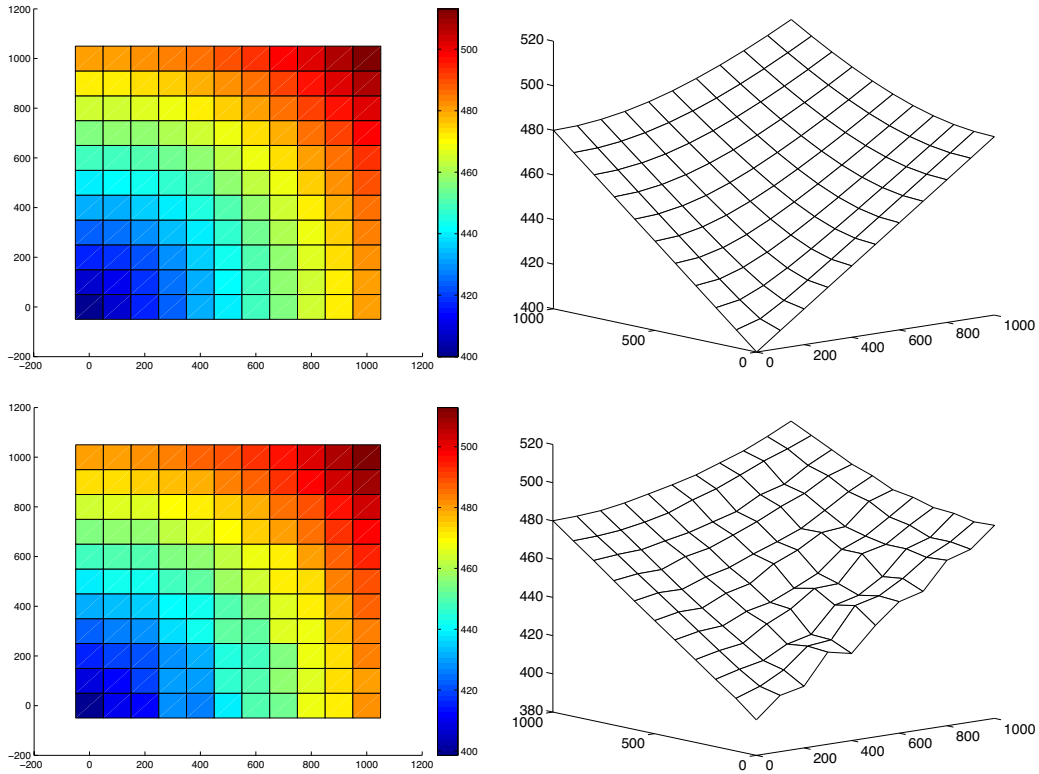


Figure 4. Top: exact $\mu(x)$ shown as (left) a contour plot and (right) a surface plot. Bottom: computed $\mu(x)$ shown as (left) a contour plot and (right) a surface plot.

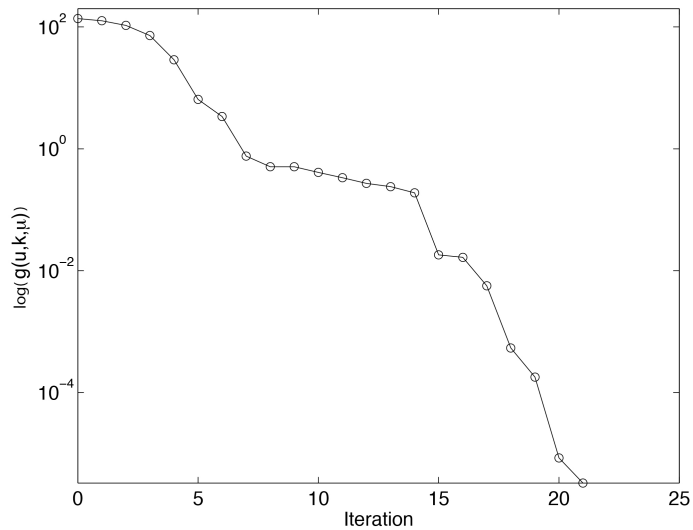


Figure 5. Convergence of the objective function per iteration for the heterogeneous problem. The y-axis is $\log(g(u, k, \mu))$.

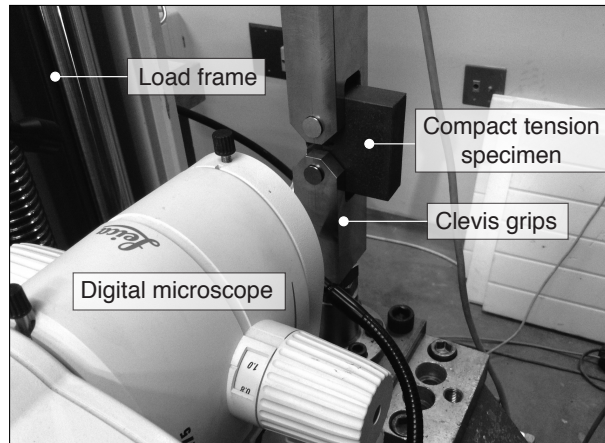


Figure 6. Experimental setup.

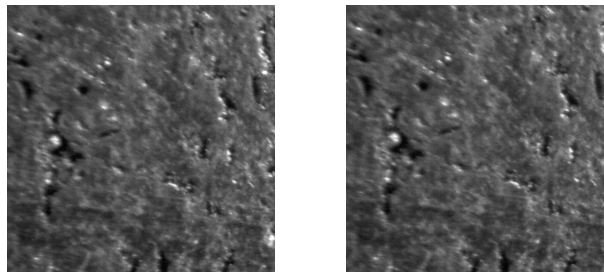


Figure 7. Left: reference image, taken prior to loading. Right: deformed image, taken early in the loading cycle. (Displacements are not visible the naked eye.)

load frame with the graphite sample loaded by clevis grips. Displacement control was used to load the sample until failure. A Leica digital microscope was used to obtain the images shown in Figure 7.⁵

Digital image correlation algorithm. The process of inverting for material parameters using digital image correlation is outlined below:

- (1) An image is taken with the microscope to serve as the reference image.
- (2) The load step is advanced.
- (3) Another image is taken to serve as the deformed image.
- (4) Control points are established for the reference and deformed images.
- (5) Displacements are calculated using a correlation algorithm (these will serve as the observed displacements, u^*).
- (6) A computational mesh is constructed such that each cell corresponds to a control point from the image correlation.

⁵It was not necessary to apply a speckle pattern to the sample since there is enough variation in surface due to the natural voids in the graphite.

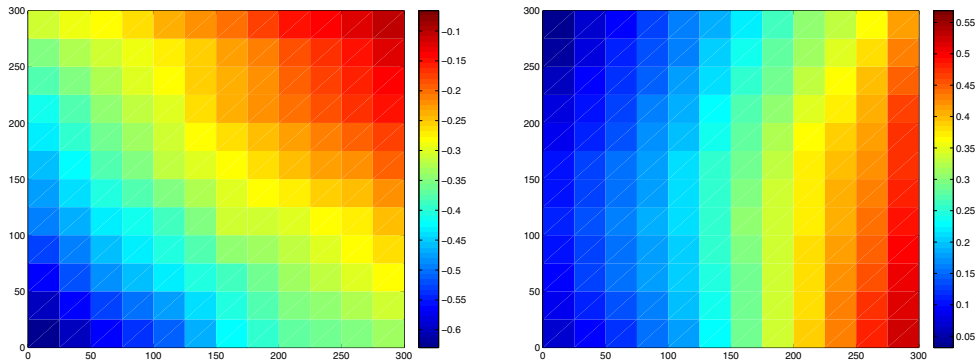


Figure 8. Left: x -displacements (px) calculated using digital image correlation. Right: y -displacement (px).

- (7) Along the outer boundary of the domain, the observed displacements are prescribed as a boundary condition for the inverse analysis.
- (8) The material parameters are seeded with values of 1.0.
- (9) The peridynamics model is inverted for k and μ until the objective function is minimized (the computed displacements from the peridynamics model match the observed image correlation displacements).

The differential method presented in [Sutton et al. 2009] was used to perform the image correlation. Bilinear interpolation was used to achieve subpixel accuracy. The digital microscope was calibrated such that 1 pixel is equivalent to 0.0147 mm. A mesh spacing of 50 pixels was used for the computed results for both the image correlation and the inverse analysis. The experimental displacements, calculated by the image correlation algorithm are shown in Figure 8.

The material parameters determined by the inverse analysis are presented in Table 2 and the error in the computed displacements is shown in Figure 9. Table 2 also shows the range of reported values in the literature. Note that the inverted material parameters fall within the reported range. Using the inverted

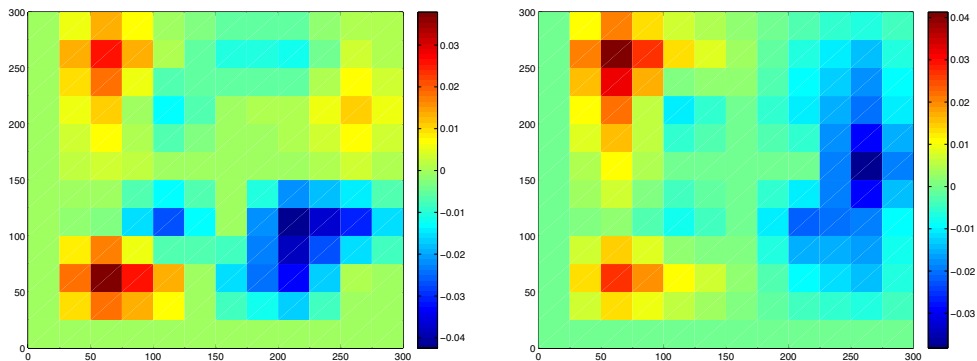


Figure 9. Left: error in the x -displacements (px) calculated using the inverted material parameters. Right: y -displacement error (px).

Parameter	Reported Range (GPa)	Computed (GPa)
k	2.3–15.3	9.18
μ	1.7–11.5	6.77

Table 2. Results for inversion problem using digital image correlation.

material parameters, Poisson’s ratio is calculated as $\nu = 0.204$ which is close to the value of $\nu = 0.2$ commonly used for nuclear graphite.

5. Inversion for load state given fracture parameters

The framework presented above can also be used to determine the state of loading given observed fracture parameters such as the crack aperture. Consider an alternative objective function given as

$$g(h) = \frac{1}{2} \sum_{j=1}^{N_{\text{obs}}} \int_{\Omega} (h - h^*)^2 \delta(\mathbf{x} - \mathbf{x}_j) d\mathbf{x} \tag{28}$$

where h^* is the measured value of the crack aperture at location \mathbf{x}_j and h is the computed crack aperture in the simulation. The decision variable in this case is the loading applied to the material, $\mathbf{d} = [F_y]$. Under these modifications, we optimize for the loading that results in a fracture with the same aperture as the observed value.

The geometry and boundary conditions for this problem are shown in Figure 10. The material parameters are given as $k = 66.7$ GPa and $\mu = 40$ GPa. The initial crack length, a was 1.0mm. The boundary conditions include a constant applied loading, F_y applied to a strip of width 2δ along the top of the domain. The displacement was constrained along a strip of width 2δ along the bottom of the domain.

A comparison of the inverted value for the loading given the crack aperture is shown in Figure 11. The observed values for the crack aperture were obtained by solving the forward problem for various magnitudes of the loading F_y and taking the relative distance between points on either side of the resulting fracture. A critical stretch damage model was used in the forward problem in which bonds that are stretched beyond a critical stretch break and no longer contribute to the material stiffness. The critical

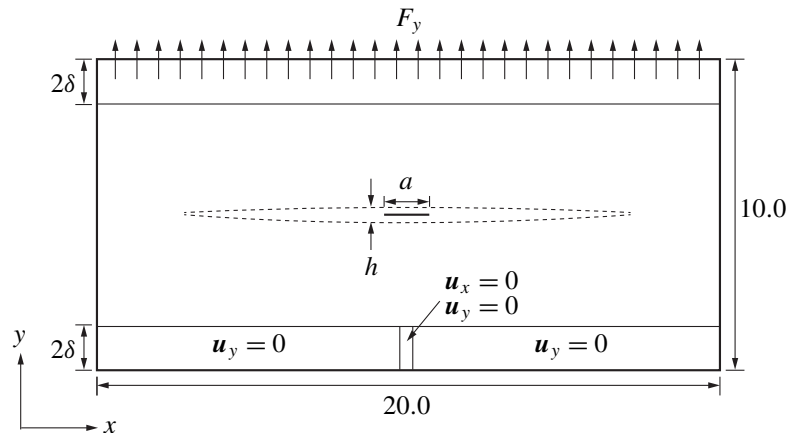


Figure 10. Geometry and boundary conditions for the load state inversion problem.

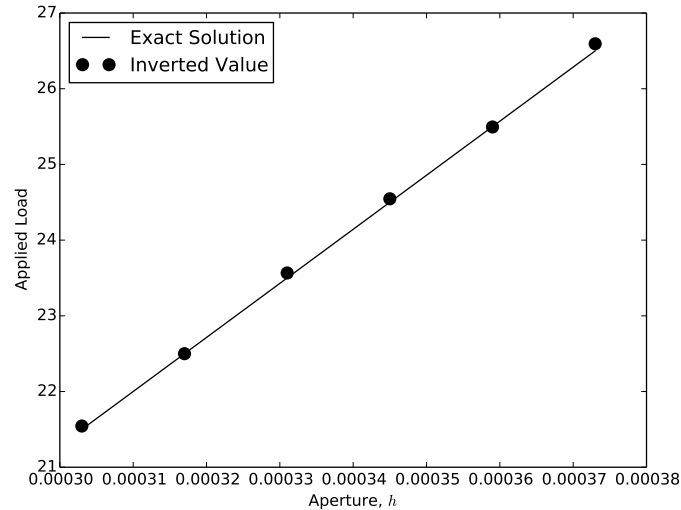


Figure 11. Inverted load state vs. exact value for the load state inversion problem.

stretch value for this problem was 0.001. The exact solution for the applied loading is represented by the loading used in the forward problem to obtain the observed crack apertures. The inverted value for the load state matches closely the exact solution suggesting that this approach to inverting for the load state is quite robust. Note that our inversion approach can solve for material properties in this dataset with minimal effort.

6. Conclusions

We have presented an adjoint-based methodology for peridynamics inverse problems and shown by means of several numerical examples, that this method can be used effectively to determine material properties for heterogeneous materials. We have also presented a framework for determining material properties that integrates digital image correlation with peridynamics inverse analysis. We have illustrated that this framework can be used to determine the load state of a material given observed fracture parameters such as the crack aperture. This peridynamics inversion capability can be used in a variety of engineering applications and provides a robust method to calibrate peridynamical models from sparse field or experimental measurements. While the solution of inverse problems in finite-element PDE based approaches may pose challenges associated with fractures, peridynamics presents a natural environment for inverse problems with discontinuities.

Acknowledgments

Sandia National Laboratories is a multiprogram laboratory managed and operated by Sandia Corporation, a wholly owned subsidiary of Lockheed Martin Corporation, for the U.S. Department of Energy's National Nuclear Security Administration under contract DE-AC04-94AL85000.

The authors would like to thank Thorsten Becker, Johan Conradie, and Matt Molteno from Stellenbosch University for their assistance with the nuclear graphite experiments. Portions of this work were funded by the Institute for Structural Engineering at Stellenbosch University.

References

- [Akçelik et al. 2006] V. Akçelik, G. Biros, O. Ghattas, J. Hill, D. Keyes, and B. van Bloemen Waanders, “Parallel algorithms for PDE-constrained optimization”, pp. 291–322 in *Parallel processing for scientific computing*, edited by M. A. Heroux et al., Society for Industrial and Applied Mathematics, Philadelphia, 2006.
- [Alali et al. 2014] B. Alali, K. Liu, and M. Gunzburger, “A generalized nonlocal calculus with application to the peridynamics model for solid mechanics”, preprint, 2014. arXiv 1402.0271v1
- [Asmaro 2013] W. P. Asmaro, *Identification of concrete fracture parameters using digital image correlation and inverse analysis*, Ph.D. thesis, University of Windsor, 2013, Available at <http://scholar.uwindsor.ca/etd/4952>.
- [van Bloemen Waanders et al. 2005] B. G. van Bloemen Waanders, R. A. Bartlett, S. S. Collis, E. R. Keiter, C. C. Ober, T. M. Smith, V. Akcelik, O. Ghattas, J. C. Hill, M. Berggren, M. Heinkenschloss, and L. C. Wilcox, “Sensitivity technologies for large scale simulation”, technical report SAND2004-6574, Sandia National Laboratories, 2005.
- [Chu et al. 1985] T. C. Chu, W. F. Ranson, M. A. Sutton, and W. H. Peters, “Applications of digital-image-correlation techniques to experimental mechanics”, *Exp. Mech.* **25**:3 (1985), 232–244.
- [Du et al. 2013a] Q. Du, M. Gunzburger, R. B. Lehoucq, and K. Zhou, “Analysis of the volume-constrained peridynamic Navier equation of linear elasticity”, *J. Elasticity* **113**:2 (2013), 193–217.
- [Du et al. 2013b] Q. Du, M. Gunzburger, R. B. Lehoucq, and K. Zhou, “A nonlocal vector calculus, nonlocal volume-constrained problems, and nonlocal balance laws”, *Math. Models Methods Appl. Sci.* **23**:3 (2013), 493–540.
- [Grédiac 2004] M. Grédiac, “The use of full-field measurement methods in composite material characterization: interest and limitations”, *Compos. Part A Appl. S.* **35**:7–8 (2004), 751–761.
- [Gunzburger and Lehoucq 2010] M. Gunzburger and R. B. Lehoucq, “A nonlocal vector calculus with application to nonlocal boundary value problems”, *Multiscale Model. Simul.* **8**:5 (2010), 1581–1598.
- [Hild and Roux 2006] F. Hild and S. Roux, “Digital image correlation: from displacement measurement to identification of elastic properties – a review”, *Strain* **42**:2 (2006), 69–80.
- [Le et al. 2014] Q. V. Le, W. K. Chan, and J. Schwartz, “A two-dimensional *ordinary*, state-based peridynamic model for linearly elastic solids”, *Internat. J. Numer. Methods Engrg.* **98**:8 (2014), 547–561.
- [Mengesha and Du 2014] T. Mengesha and Q. Du, “Nonlocal constrained value problems for a linear peridynamic Navier equation”, *J. Elasticity* **116**:1 (2014), 27–51.
- [Mengesha and Du 2015] T. Mengesha and Q. Du, “On the variational limit of a class of nonlocal functionals related to peridynamics”, *Nonlinearity* **28**:11 (2015), 3999–4035.
- [Pan et al. 2009] B. Pan, K. Qian, H. Xie, and A. Asundi, “Two-dimensional digital image correlation for in-plane displacement and strain measurement: a review”, *Meas. Sci. Technol.* **20**:6 (2009), 062001.
- [Périeré et al. 2009] J. N. Périeré, H. Leclerc, S. Roux, and F. Hild, “Digital image correlation and biaxial test on composite material for anisotropic damage law identification”, *Int. J. Solids and Struct.* **46**:11–12 (2009), 2388–2396.
- [Silling 2000] S. A. Silling, “Reformulation of elasticity theory for discontinuities and long-range forces”, *J. Mech. Phys. Solids* **48**:1 (2000), 175–209.
- [Silling and Askari 2005] S. A. Silling and E. Askari, “A meshfree method based on the peridynamic model of solid mechanics”, *Comput. Struct.* **83**:17–18 (2005), 1526–1535.
- [Silling and Lehoucq 2008] S. A. Silling and R. B. Lehoucq, “Convergence of peridynamics to classical elasticity theory”, *J. Elasticity* **93**:1 (2008), 13–37.
- [Silling et al. 2007] S. A. Silling, M. Epton, O. Weckner, J. Xu, and E. Askari, “Peridynamic states and constitutive modeling”, *J. Elasticity* **88**:2 (2007), 151–184.
- [Sutton et al. 2009] M. A. Sutton, J.-J. Orteu, and H. W. Schreier, *Image correlation for shape, motion and deformation measurements: basic concepts, theory and applications*, Springer, New York, 2009.
- [Tikhonov and Arsenin 1977] A. N. Tikhonov and V. Y. Arsenin, *Solutions of ill-posed problems*, Winston, Washington, DC, 1977.

Received 26 Nov 2014. Revised 5 Nov 2015. Accepted 7 Nov 2015.

DANIEL Z. TURNER: dzturne@sandia.gov

Multiscale Science, Sandia National Laboratories, P.O. Box 5800, Albuquerque, NM 87185, United States

BART G. VAN BLOEMEN WAANDERS: bartv@sandia.gov

Optimization and UQ, Sandia National Laboratories, P.O. Box 5800, Albuquerque, NM 87185, United States

MICHAEL L. PARKS: mlparks@sandia.gov

Computational Mathematics, Sandia National Laboratories, P.O. Box 5800, Albuquerque, NM 87185, United States

JOURNAL OF MECHANICS OF MATERIALS AND STRUCTURES

msp.org/jomms

Founded by Charles R. Steele and Marie-Louise Steele

EDITORIAL BOARD

ADAIR R. AGUIAR	University of São Paulo at São Carlos, Brazil
KATIA BERTOLDI	Harvard University, USA
DAVIDE BIGONI	University of Trento, Italy
YIBIN FU	Keele University, UK
IWONA JASIUK	University of Illinois at Urbana-Champaign, USA
C. W. LIM	City University of Hong Kong
THOMAS J. PENCE	Michigan State University, USA
DAVID STEIGMANN	University of California at Berkeley, USA

ADVISORY BOARD

J. P. CARTER	University of Sydney, Australia
D. H. HODGES	Georgia Institute of Technology, USA
J. HUTCHINSON	Harvard University, USA
D. PAMPLONA	Universidade Católica do Rio de Janeiro, Brazil
M. B. RUBIN	Technion, Haifa, Israel

PRODUCTION production@msp.org

SILVIO LEVY Scientific Editor

Cover photo: Wikimedia Commons

See msp.org/jomms for submission guidelines.

JoMMS (ISSN 1559-3959) at Mathematical Sciences Publishers, 798 Evans Hall #6840, c/o University of California, Berkeley, CA 94720-3840, is published in 10 issues a year. The subscription price for 2015 is US\$565/year for the electronic version, and \$725/year (+\$60, if shipping outside the US) for print and electronic. Subscriptions, requests for back issues, and changes of address should be sent to MSP.

JoMMS peer-review and production is managed by EditFLOW® from Mathematical Sciences Publishers.

PUBLISHED BY

 **mathematical sciences publishers**
nonprofit scientific publishing

<http://msp.org/>

© 2015 Mathematical Sciences Publishers

